Thermal Effects on Critical Flow Venturis

John D. Wright: National Institute of Standards and Technology (NIST)
Woong Kang: Korea Research Institute of Standards and Science (KRISS)
Liang Zhang: National Institute of Metrology – China (NIM)
Aaron N. Johnson and Michael R. Moldover: NIST
Corresponding Author: john.wright@nist.gov

$A_{\mathrm{ref}} = \pi {d_{\mathrm{ref}}}^2/4$	CFV throat area at reference temperature
$Bi = h\,\ell/k$	Biot number, ratio of convective to conductive heat flux resistance
$C_{\mathrm{d}} = \dot{m}_{\mathrm{ref}}/\dot{m}_{\mathrm{CFV}}$	Experimental CFV discharge coefficient
C_{inv}	Correction to CFV 0$^{\mathrm{th}}$ order model for the inviscid, core flow
C_{T}	Correction to CFV 0$^{\mathrm{th}}$ order model for the thermal boundary layer
C_{α}	Correction to CFV 0$^{\mathrm{th}}$ order model for throat thermal expansion
C_{vbl}	Correction to CFV 0$^{\mathrm{th}}$ order model for the velocity boundary layer
C_{R}^{*}	Real gas critical flow factor (calculated from a thermodynamic database [1])
d_{ref} or d	CFV throat diameter at reference temperature
h	Convective heat transfer coefficient at the CFV interior wall
k	Material conductive heat transfer coefficient
ℓ	Distance from the CFV interior wall to the CFV exterior wall
M	Gas molar mass
Ma	Mach number
$\dot{m}_{\mathrm{R}*} = C_{\mathrm{R}}^{*} P_0 A\sqrt{M}/\sqrt{RT_0}$	0$^{\mathrm{th}}$ order CFV mass flow, accounting only for real gas effects
$\dot{m}_{\mathrm{ref}}$	Mass flow measured with a reference flow standard
$\dot{m}_{\mathrm{CFV}}$	Mass flow through a CFV calculated by theoretical or analytical means
P_0	Stagnation pressure at the CFV approach pipe
$Re = \dfrac{4\dot{m}}{\pi d \mu_0}$	Reynolds number, using the throat diameter as length scale, μ_0 is the dynamic viscosity based on P_0 and T_0
R	Universal gas constant
T_0	Stagnation temperature in the CFV approach pipe
T_{aw}	CFV wall temperature assuming an adiabatic condition between the wall and the flowing gas
T_{body}	Actual CFV body temperature
T_{core}	Temperature of the core flow
T_{ref}	Reference temperature used for the throat dimensions
T_{room}	Room temperature
T_{wall}	CFV interior wall temp
T_{surf}	CFV exterior wall temp
ΔT	$T_{\mathrm{wall}} - T_0 \approx T_{\mathrm{body}} - T_0$
T_z	Temperature measured at axial position z = 10 mm upstream from CFV inlet
α	Linear coefficient of thermal expansion for the CFV body material
K	Dimensionless proportionality constant between $Re^{-1/2}\,(\Delta T)/T_{\mathrm{ref}}$ and C_T
Ω	CFV inlet curvature ratio, ≈ 0.25 for standard CFV geometry

Abstract

Critical flow venturis (CFVs) are widely used as working and transfer standards for gas flow measurement because of their long-term calibration stability (< 0.06 %) and well developed physical model. At Reynolds numbers *Re* < 2.5 x 10^5 (*e.g.*, a 2 mm throat diameter flowing air at 1 MPa), CFVs exhibit sensitivity to the environmental temperature of approximately 200 parts in 10^6/ K, primarily due to the difficulty of measuring the temperature of the gas entering the CFV (temperature "sampling" errors) and thermal boundary layer effects. For example, during the CCM.FF-K6 2002 key comparison [2], the temperature sensitivity of the CFV transfer standard accounted for as much as 40 % of the transfer standard uncertainty. Heat transfer from the CFV body to the thermal boundary layer produces an annular region of lower density gas near the CFV wall and a lower CFV discharge coefficient. We minimized temperature sampling errors by using a better gas temperature measurement design, including non-metallic approach pipe materials and a temperature sensor with low stem conduction error. We measured and accounted for thermal boundary layer effects using the correction $C_T = 1 + KRe^{-1/2}[\Delta T/T_0]$ where ΔT is the difference between the CFV inner wall temperature and the inlet gas temperature. The value of K is approximately -7 for CFVs made of stainless steel and copper with diameters of 0.56 mm, 1.1 mm, and 3.2 mm for the particular CFV configuration we used.

1. Introduction to Critical Flow Venturis

Toroidal critical flow venturis (CFVs) have a contracting inlet with radius of curvature approximately twice the throat diameter followed by a conical outlet [3], see Figure 1a. If a critical pressure ratio is maintained across the CFV (conservatively $P_{\mathrm{down}}/P_0 < 0.5$ for air), the gas expands to sonic velocity at the throat. The commonly used "0th order" physical model assumes isentropic flow and adiabatic wall conditions to calculate mass flow $\dot{m}_{\mathrm{R}*}$ from the upstream stagnation pressure P_0 and temperature T_0:

$$\dot{m}_{\mathrm{R}*} = C_{\mathrm{R}}^* \frac{P_0 A_{\mathrm{ref}} \sqrt{M}}{\sqrt{RT_0}} \ , \qquad (1)$$

where $A_{\mathrm{ref}} = \pi {d_{\mathrm{ref}}}^2/4$ is the throat area, C_{R}^* is the real critical flow factor (calculated from a thermodynamic database [1]), M is the gas molar mass, and R is the universal gas constant [4].[1] Most users calibrate their CFV against a reference flow standard over a range of P_0 values and calculate a discharge coefficient $\dot{m}_{\mathrm{ref}}/\dot{m}_{\mathrm{R}*}$. Alternatively, if the CFV inlet shape and throat diameter dimensions are well known, analytical calculations of the corrections C_{inv} and C_{vbl} give excellent agreement with experimental data (except near the laminar-to-turbulent transition). Hall in 1962 [5] and Kliegel and Levine in 1969 [6] calculated inviscid core flow corrections (C_{inv}) that reduce the 0th order mass flow for the standard shaped CFV by 0.12 % for all CFV sizes and flows. For most CFV flows (*Re* < 10^9), the departure of $\dot{m}_{\mathrm{ref}}/\dot{m}_{\mathrm{R}*,\mathrm{inv}}$ from the ideal value of unity is primarily due to the thickness of the velocity boundary layer at the wall: the lower velocities in the boundary layer reduce the mass flux relative to the assumption of sonic velocity across the entire throat. Tang in 1969 [7] and Geropp in 1971 [8]

[1] Note that C_{I}^* is sometimes used (calculated from the gas specific heat ratio as a function of pressure and temperature) but C_{R}^* better accounts for real gas effects.

published similarity transformations to calculate corrections for the laminar boundary layer effects for an adiabatic wall (C_{vbl}). Stratford in 1964 [9] and Mickan in 2006 [10] used an integral boundary layer technique to predict C_{vbl} for a turbulent boundary layer. Because the laminar boundary layer thickness scales with $Re^{-1/2}$, experimental $\dot{m}_{\mathrm{ref}}/\dot{m}_{\mathrm{R*,inv,vbl}}$ values are nearly linearized when plotted versus $Re^{-1/2}$. In this study, the Reynolds numbers are all less than the normal transition value of 1 x 10^6 and therefore are laminar. Because the interactions between the various phenomena (C_{inv}, C_{vbl}, etc.) are weak, we use Composite Linear CFV theory [11] and simply multiply correction ratios from various sources to calculate an overall effect.

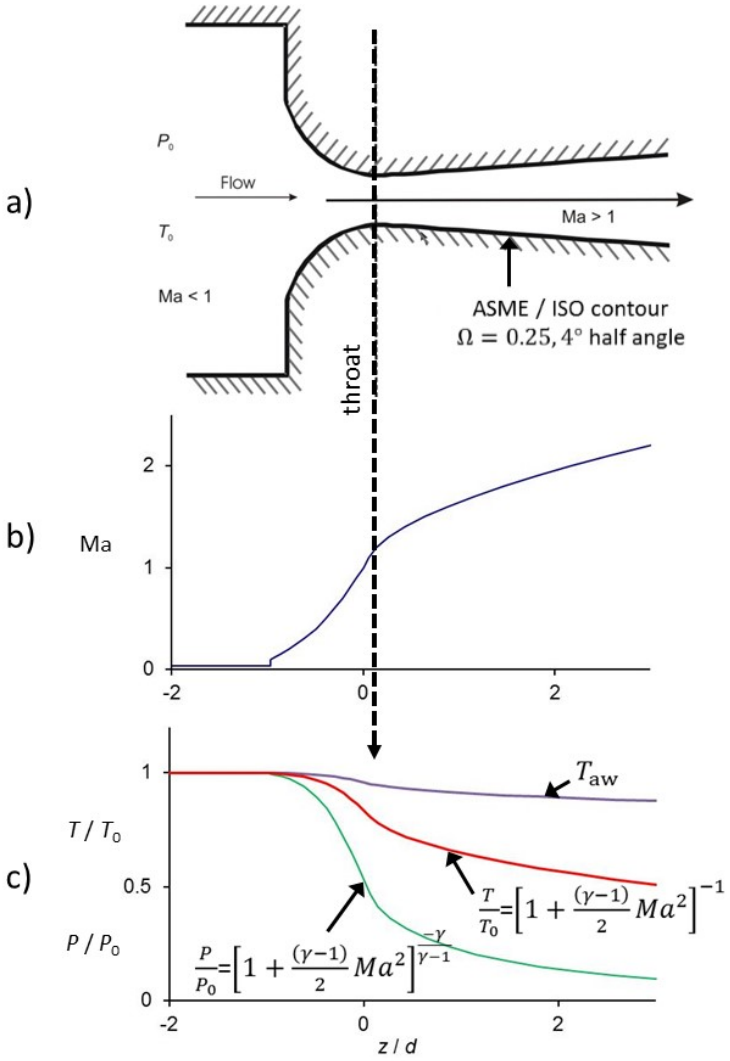

Figure 1. a) Shape of an ISO 9300 toroidal CFV, b) Mach number *Ma* in the core flow assuming fully expanded, one-dimensional, inviscid, and isentropic flow of a perfect gas with an adiabatic wall, and c) ideal, normalized free stream pressure, free stream temperature, and adiabatic wall temperature. (Assumes temperature recovery factor = 0.75.) Rapid expansion through the throat leads to Mach numbers > 1 and rapid decreases in pressure and temperature.

2. A Note about Nomenclature

There are too many definitions of C_d! It is clear that it is a ratio of an experimentally measured or reference flow to a theoretically calculated flow according to the CFV, i.e.,

$$C_\mathrm{d} = \frac{\dot{m}_\mathrm{ref}}{\dot{m}_\mathrm{CFV}} . \tag{2}$$

But the definition of $\dot{m}_\mathrm{CFV}$ is not consistent in the literature.

Herein, we will represent corrections for the various proposed effects using the following subscripts: 1) **R*** for the real gas property effects [1], 2) **inv** for the inviscid core flow effects, 3) **vbl** for the velocity boundary layer effects with an adiabatic wall, 4) $\boldsymbol{\alpha}$ for the effects of throat thermal expansion, and 5) **T** for the effects of the thermal boundary layer with heat transfer from the CFV wall. By this nomenclature system, $\dot{m}_{\mathrm{R}*,\mathrm{inv},\mathrm{vbl},\alpha,\mathrm{T}} = C_\mathrm{inv} C_\mathrm{vbl} C_\alpha C_\mathrm{T}\ \dot{m}_{\mathrm{R}*}$. In prior CFV publications, C_d usually represents $C_\mathrm{inv} C_\mathrm{vbl}$. We will not use the variable C_d hereafter, but rather a more specific description such as $C_\mathrm{R}^* C_\mathrm{inv} C_\mathrm{vbl}$, or $C_\mathrm{R}^* C_\mathrm{inv} C_\mathrm{vbl} C_\alpha C_\mathrm{T}$ which will be the basis for CFV theoretical mass flow calculations in this publication, such as $\dot{m}_{\mathrm{R}*,\mathrm{inv},\mathrm{vbl}}$ or $\dot{m}_{\mathrm{R}*,\mathrm{inv},\mathrm{vbl},\alpha,\mathrm{T}}$.

3. Why Study CFVs?

Critical flow venturis are widely used as working standards and transfer standards because of their excellent calibration stability and well understood physics.

3.1 Long Term Calibration Stability: In prior work [12], we found calibration stability of 0.2 % for a population of 23 CFVs, some over 26 years. But the low uncertainty (0.025 %, *k*=2) of newer gas flow standards and pressure sensors [13] give CFV stability better than 300 parts in 10^6 over 4 or more years (Figure 2). Hence, CFVs are used as working standards to transfer primary standard traceability to other flow meters with only small additional uncertainty. Secondary laboratories can use working standard CFVs as flow references, achieving uncertainties < 0.1 % [14, 15] without the traceability and maintenance complexities of a primary standard (e.g. a piston or bell prover).

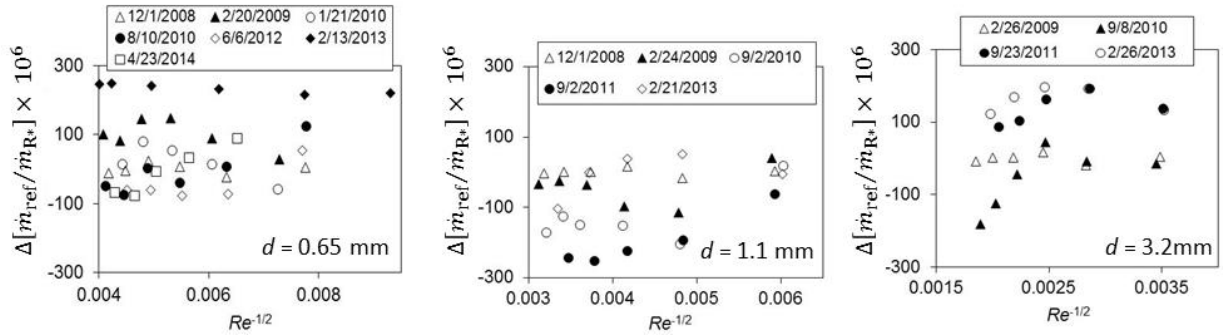

Figure 2. Calibration stability (with respect to an initial calibration) for three NIST working standard CFVs with *d* = 0.65 mm, 1.1 mm, and 3.2 mm.

3.2 Well Understood Physical Model: Experimentalists have gathered low uncertainty dimensional and flow measurements of CFVs and thereby confirmed that the analytically calculated $C_{\mathrm{R}}^{*}C_{\mathrm{inv}}C_{\mathrm{vbl}}$ values for the laminar flow regime are correct within 0.05 % [16, 11**Error! Bookmark not defined.**]. This is an exceptionally accurate application of fluid mechanics to a real world flow problem that elevates the CFV to the most economical method for measuring large flows with low uncertainty.

CFVs are often used as transfer standards during laboratory comparisons because 1) they have excellent calibration stability, and 2) the well-developed physical model that accounts for their sensitivity to gas properties and the gas temperature. However, smaller nozzles (< 10 mm) show significant environmental temperature sensitivity. During the CCM.FF-K6 2002 key comparison [2], the temperature sensitivity of the CFV transfer standard accounted for 40 % of the uncertainty contributed by the transfer standard at the lower flows of the comparison [17].

Figure 3 shows a 5-fold improvement in CFV flow measurements when the thermal effect corrections described herein are applied to a *d* = 0.58 mm CFV. It shows the change in CFV mass flow relative to reference values that have uncertainty of 0.05 %. The flow was measured by the reference and by a CFV subjected to temperature changes from 296 K to 303 K and back to 296 K. Using the normal approach to calculate flow through the CFV ($\dot{m}_{\mathrm{CFV}} = C_{\mathrm{inv}}C_{\mathrm{vbl}}\ \dot{m}_{\mathrm{R}*}$), the 7 K room temperature change leads to a flow measurement error of 0.12 %. Correcting for thermal expansion of the CFV material ($\dot{m}_{\mathrm{CFV}} = C_{\mathrm{inv}}C_{\mathrm{vbl}}C_{\alpha}\ \dot{m}_{\mathrm{R}*}$) increases the flow measurement error to 0.14 %. By introducing a correction for thermal boundary layer effects ($\dot{m}_{\mathrm{CFV}} = C_{\mathrm{inv}}C_{\mathrm{vbl}}C_{\alpha}C_{\mathrm{T}}\ \dot{m}_{\mathrm{R}*}$), the errors are < 0.01 %, except during the periods of rapidly changing room temperature where they are as large as 0.025 %.

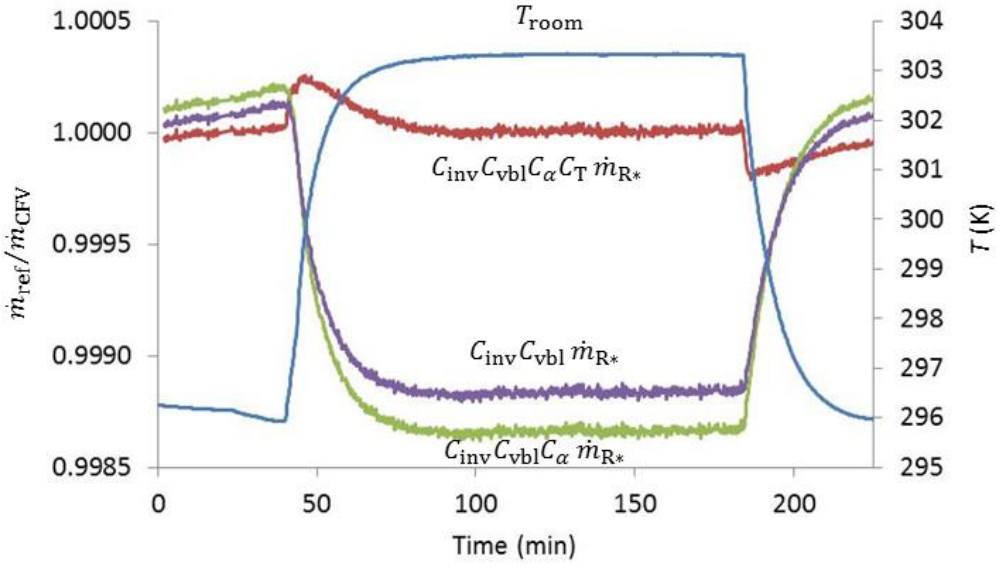

Figure 3. Step changes in the room temperature (T_{room}) and the resulting flow measurement errors for a *d*= 0.58 mm CFV versus time for three CFV flow models. The data labelled $C_{\mathrm{inv}}C_{\mathrm{vbl}}C_{\alpha}\ \dot{m}_{\mathrm{R}*}$ represents the normally used CFV flow calculation model and the data labelled $C_{\mathrm{inv}}C_{\mathrm{vbl}}C_{\alpha}C_{\mathrm{T}}\ \dot{m}_{R*}$ (red curve) show the results when the thermal corrections described in this paper are applied.

4. Introduction to Thermal Effects on CFVs

Early studies of thermal effects on CFVs used relatively large CFVs (d ≈ 25 mm) where thermal boundary layer effects are not significant because the thermal boundary layer comprised such a small portion of the throat area [18, 19, 20]. The researchers were interested in the temperature profile within the CFV and the best location to measure the CFV body temperature to account for the thermal expansion of the throat area.

Bignell and Choi [21] experimentally quantified thermal boundary layer effects by measuring and controlling CFV body temperature and measuring the resulting changes in the CFV flow. Our experimental results are compared with those of Bignell and Choi in Figure 17.

Wright [17] listed the following categories for CFV temperature sensitivity sources in order of increasing importance for CFVs operating in the laminar regime (generally smaller than d = 10 mm): 1) sensitivity of reference sensors to room T changes, e.g. the mass flow reference, the pressure sensor measuring P_0, 2) thermal expansion of the throat area, 3) the thermal boundary layer, and 4) temperature "sampling errors".

1) *Reference sensor sensitivity:* For the experiments presented herein, the room T was 297.3 K ± 0.3 K. The temperature sensitivity of the CFV pressure transducer was negligible (< 0.01 %). The reference flow standards (the 34 L and 677 L *PVTt* [13]) are in a temperature controlled water bath and also have negligible temperature sensitivity for the purposes of these experiments.

2) *Thermal expansion of the CFV throat area:* The accepted correction for thermal expansion of the CFV throat is:

$$C_\alpha = \frac{A}{A_{\mathrm{ref}}} = 1 + 2\,\alpha\left(T_{\mathrm{body}} - T_{\mathrm{ref}}\right), \tag{3}$$

where A_{ref} is the throat area at the reference temperature 298.15 K, α is the linear coefficient of thermal expansion, and T_{body} and T_{ref} are the actual CFV body temperature and the reference temperature used for the throat dimensions respectively. The thermal expansion effect is $2\,\alpha$ = 34 x 10^{-6} K^{-1} for both stainless steel and for the Cu-Te alloy 145 and 9 x 10^{-6} K^{-1} for the machinable ceramic used to make the CFVs in this study. Thermal expansion is significant for CFVs with d > 10 mm, but for the 3.2 mm or smaller CFVs in this study, thermal boundary layer effects are 5 times larger. Furthermore, since thermal expansion and thermal boundary layer effects are opposite in sign, applying C_α without applying thermal boundary layer corrections (C_T) makes flow results worse rather than better. In this study, C_α was applied to the results in order to isolate thermal boundary layer effects.

3) *Thermal boundary layer:* Warmer, lower density gas near the CFV wall reduces mass flux through the CFV, an effect that increases in significance at lower Reynolds numbers (smaller CFVs). Johnson *et. al.* [22] presented computational fluid dynamics results showing a decrease in $C_{\mathrm{inv}}C_{\mathrm{vbl}}$ for a CFV wall warmer than the adiabatic wall temperature due to a thermal boundary layer. They also noted that the mass flux change is predominantly due to density changes (only weakly due to velocity

changes), and that the magnitude of the thermal boundary layer effect is proportional to $Re^{-1/2}$ and to the gas specific heat ratio γ.

4) *Temperature sampling errors:* Ideally, we would measure the temperature of the gas averaged over the entrance surface of the converging CFV. Unfortunately, it is impractical to place a temperature sensor at the entrance to a small CFV, either because it disrupts the flow field or is too small to be robust. CFV documentary standards [3] call for the temperature sensor to be placed approximately two approach pipe diameters upstream from the CFV entrance plane, but experience shows that better temperature measurement designs are needed [17].

Figure 4 schematically represents the various thermal elements of the CFV system and the heat fluxes between them. The gas cools as it accelerates through the CFV and the gas cools the CFV body. The CFV body cools the approach pipe and the inlet gas, and often cools the gas temperature sensor by stem conduction. Heat transfer from the room complicates matters: changes in the room temperature and ventilation will lead to time-dependent and space-dependent heat fluxes on every component. The thermal time response of the entire CFV system (including the temperature sensor) is a concern regarding 1) how long one must wait to perform a steady state flow measurement or 2) the uncertainty of dynamic CFV flow measurements [23].

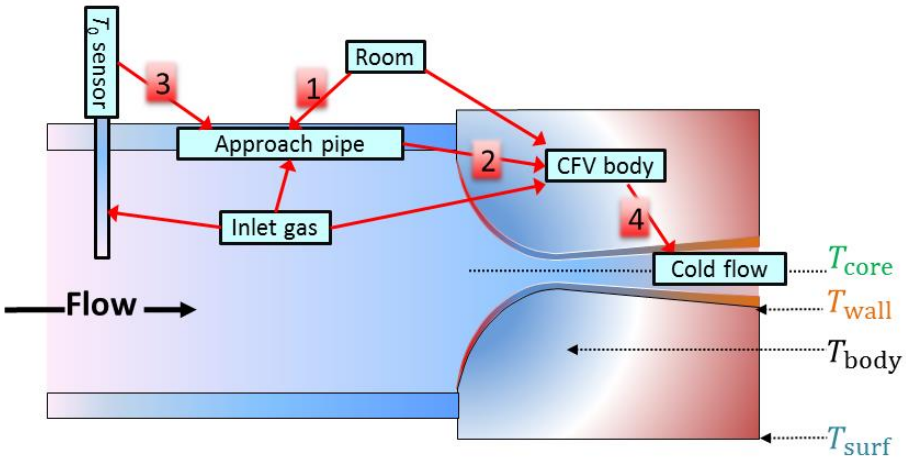

Figure 4. Measured T_0 is subject to sampling errors due to heat transfer within the flow, CFV body, and approach pipe walls. Arrows indicate typical directions of heat flux between system elements.

In the remainder of this paper we will 1) discuss the temperature distribution within the CFV body and how to obtain approximate measurements of the interior wall temperature, 2) describe a custom CFV holder and approach pipe design that reduced temperature sampling errors in our experiment to < 0.02 %, and 3) present the results of experiments in which CFV bodies made of copper, stainless steel, and ceramic were heated to four set-point temperatures to quantify thermal boundary layer effects. The objective is to present a physical model for a thermal boundary layer correction C_T to allow CFV users to make corrections for temperature effects and thereby reduce the uncertainty of CFV gas flow measurements.

5. Temperature Distribution in the Critical Flow Venturi Body

In our thermal boundary layer experiments, we tested CFVs made of stainless steel, copper, and ceramic. We made some of the CFVs of copper because of its high thermal conductivity (k_{Cu}=3.8 W/[cm K]). If the conductive heat transfer through the CFV body material is much greater than the convective heat transfer between the CFV wall and the gas flow, a temperature measurement anywhere within the CFV body is a good approximation of the CFV internal wall temperature. This makes it easier to study thermal boundary layer effects on the CFV flow. In the following sections we will describe 1) a computational model to estimate the temperature profile in the CFV, 2) a simple analytical model for the temperature, and 3) the radial temperature profile in the CFV predicted by the two models.

5.1 Computational Model: A computational fluid dynamics (CFD) code (Fluent[2]) was used to calculate the temperature distribution of the gas flowing through the CFV at the maximum tested pressure (700 kPa). The CFD solution was coupled to CFV bodies with T_{surf} = 313 K made of 1) Copper-Tellurium alloy (Cu), 2) 316 stainless steel (SS), and 3) ceramic materials to compute the temperature distribution within the CFV bodies. A laminar boundary layer was assumed for the gas flow simulation and the ends of the CFV bodies were adiabatic. Figure 5 shows the computed temperature distributions for the *d* = 3.2 mm CFVs for the three materials. The spatial pattern of temperatures in the diverging section is difficult to predict because it depends on the position of shock waves. We do not expect the CFD simulations to accurately capture the positions of shocks and other details of the flow, but they do give qualitative insight on the CFV body temperature distributions.

[2] In order to describe materials and procedures adequately, it is occasionally necessary to identify commercial products by manufacturers' name or label. In no instance does such identification imply endorsement by the National Institute of Standards and Technology, nor does it imply that the particular product or equipment is necessarily the best available for the purpose.

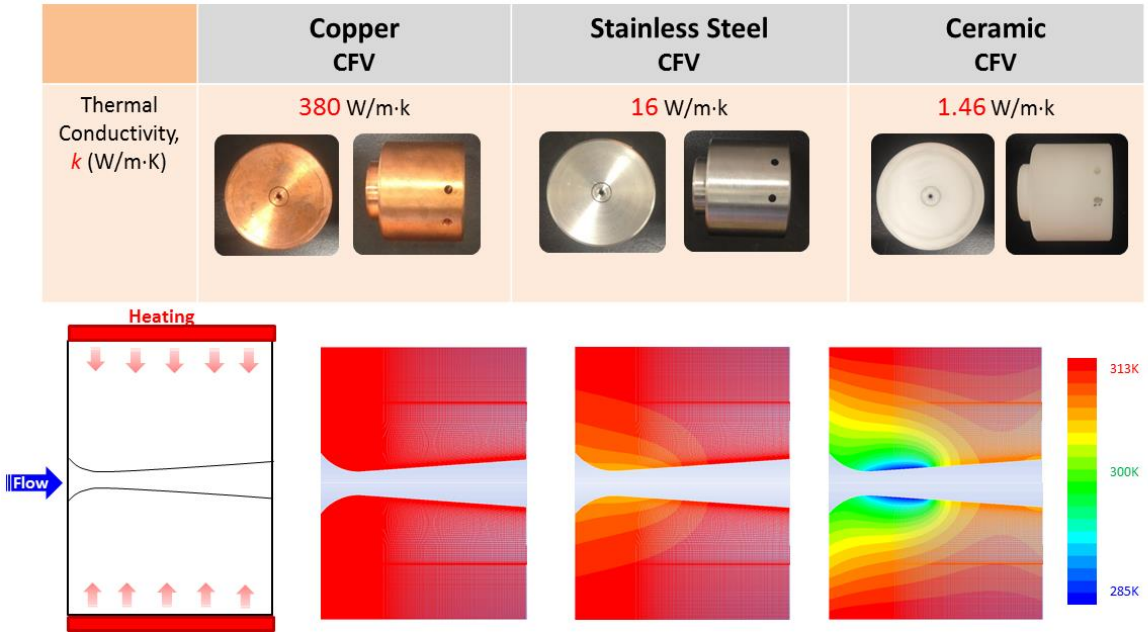

Figure 5. Temperature distribution within the CFV body from the computational model for the *d* = 3.2 mm CFVs made of three materials at stagnation pressure of 700 kPa.

5.2 Analytical Model: The analytical temperature model assumed 1-dimensional, isentropic, over-expanded (no shocks) flow to calculate the adiabatic wall temperature [4] through an ISO toroidal CFV. We assumed a constant temperature for the CFV exterior surface. We used Smith and Spalding's [24] convective heat transfer coefficient for the boundary layer and a textbook heat transfer model for cylindrical shells [25] to calculate the temperature on the CFV interior wall. To simplify calculation of the CFV material temperature, we assumed no heat transfer in the axial direction.

Figure 6 shows temperatures from the analytic model for a CFV made of stainless steel with 17.5 mm body radius and a throat diameter *d* = 3.2 mm. Figure 6 shows temperatures on a plane bisecting the CFV in the axial direction; 1) the heated CFV exterior T_{surf} = 313 K, 2) the temperature of the CFV interior wall T_{wall} , 3) the adiabatic wall temperature T_{aw} , and 4) the temperature of the gas in the free stream T_{core}. The adiabatic wall temperature is warmer than the core flow due to viscous heating in the boundary layer. The temperatures predicted by the analytical model in the radial direction at the throat cross section will be discussed in the following section along with the results from the computational model

5.3 Radial Temperature Distribution: Figures 7a and 7b show temperature profiles for radial sections at the CFV throat for a *d* = 3.2 mm and a *d* = 0.56 mm CFV respectively, for all three CFV body materials. The results from the analytical model are shown as symbols and the computational model results are shown as solid lines. The two models for the temperature in the CFV body agree to better than 1.2 K.

Figure 7 illustrates the importance of the Biot number in the thermal boundary layer experiments. The Biot number is the ratio of the resistance to conductive heat transfer inside the CFV body to the convective heat transfer resistance at the surface: $Bi = h\,\ell/k$ where h is the convective heat transfer

coefficient of the gas flowing inside the CFV, ℓ is a characteristic length of the CFV (the distance between the interior and exterior CFV walls), and k is the thermal conductivity of the CFV material. When the CFV thermal conductivity is larger (as is true for Cu relative to SS or ceramic), the Biot number is lower, and the CFV body temperature is nearly uniform and equal to the external, controlled temperature. Conversely, a larger Biot number leads to a larger temperature gradient in the CFV body. A larger flow (larger h) or less conductive CFV material will cause a larger Biot number.

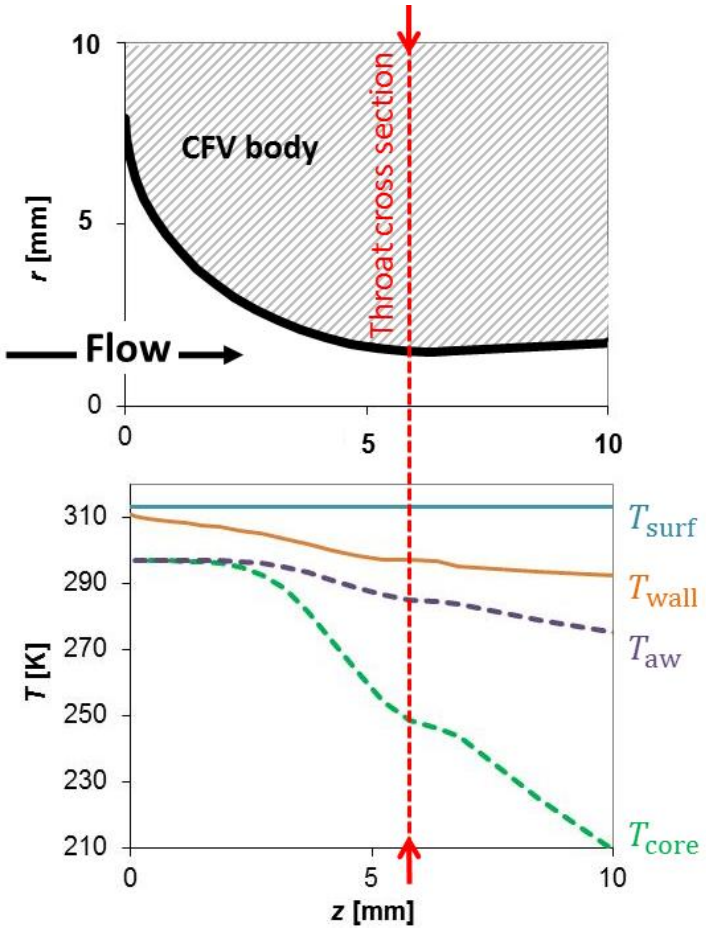

Figure 6. Analytically modeled temperature for an externally heated (T_{surf} = 313 K) *d* = 3.2 mm stainless steel CFV.

In the experimental design described in the following section, we used the temperature measured by a bead thermistor embedded in the CFV body 5.5 mm from the CFV centerline (the position indicated by T_{body} in Figure 7) to approximate the temperature of the CFV wall (T_{wall} in Figure 7). Both thermal models indicate that that $T_{body} - T_{wall}$ < 0.2 K for the Cu CFVs and < 3.9 K for the SS CFVs. However, T_{body} is not a good approximation of T_{wall} for the ceramic material: $T_{body} - T_{wall}$ is as large as 15 K. Ceramic is a good insulator and more closely approximates the adiabatic wall condition used in theoretical calculations of the discharge coefficient.

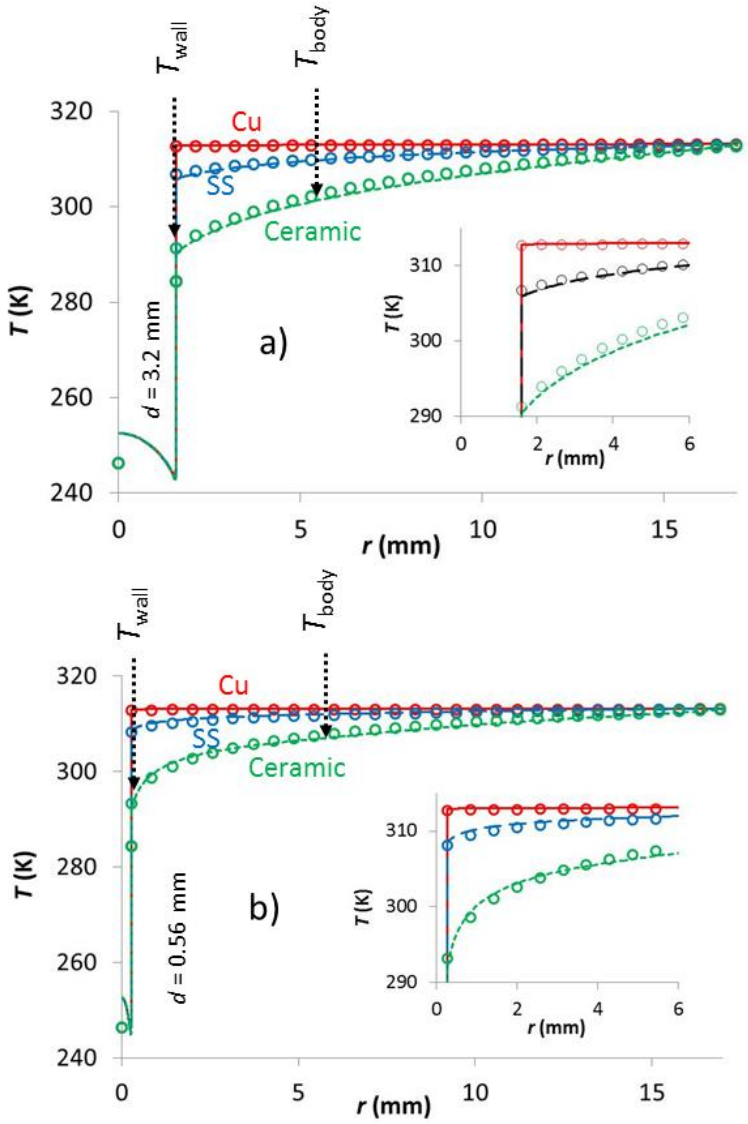

Figure 7. Radial temperature distributions at the CFV throat, Cu, SS, and ceramic materials, for the a) d = 3.2 mm and b) d = 0.56 mm CFVs. Lines are from the computational model and symbols are from the analytical model.

6. Experimental Approach

The goal of the CFV holder and approach pipe design was to accurately measure the gas temperature entering a CFV with a different body temperature. CFVs with d = 3.2 mm, 1.1 mm, and 0.65 mm were machined from Copper (Cu), stainless steel (SS), and a machinable ceramic material. The 9 CFVs were calibrated against the NIST *PVTt* flow standards using an experimental arrangement designed to minimize temperature sampling errors. The temperature of the CFV body was PID controlled at four set points by an electric heater to measure the influence of the thermal boundary layer on the CFV discharge coefficients.

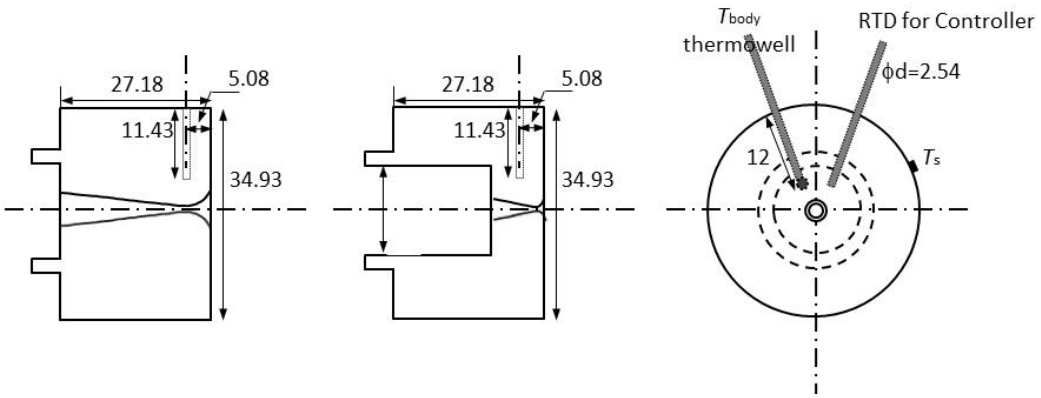

Figure 8. Construction details and locations of CFV temperature sensors for the 3.2 mm and 1.1 mm CFVs (all dimensions in mm).

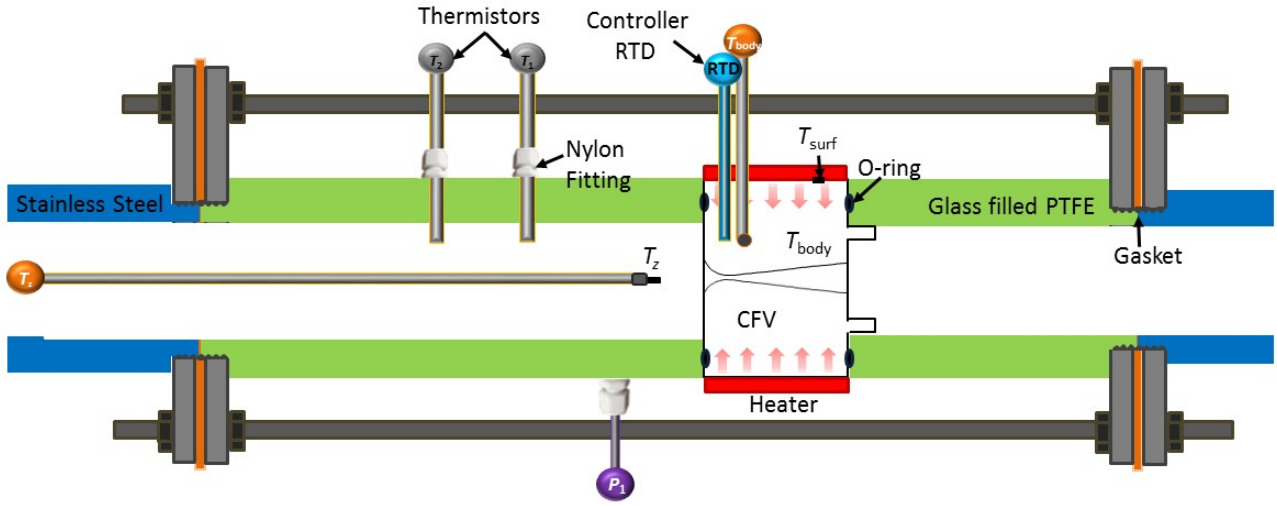

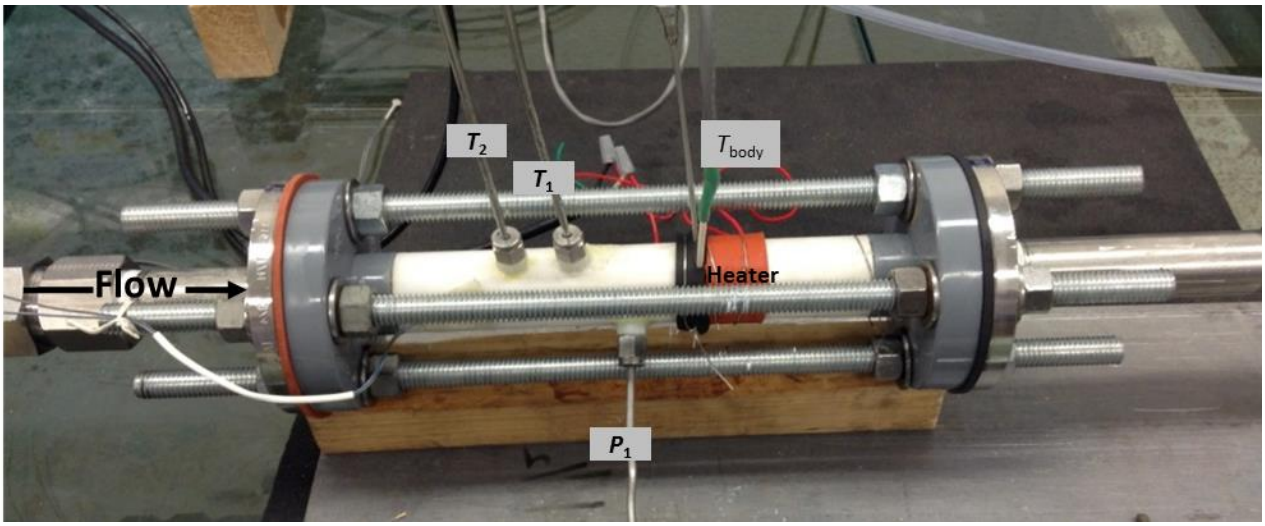

Figure 9. Experimental arrangement and locations of sensors.

Some details of the experimental design are:

1) Thermostatted bath water was pumped through a plate heat exchanger to condition the incoming gas to match the nominal room temperature of 296.7 K and thereby minimize heat transfer from the room through the approach pipe walls. The CFV inlet gas temperatures were 297 K ± 0.7 K during tests. The room temperature measured by a thermistor 1 m away from the test section was 297 K ± 0.3 K through all of the thermal boundary layer tests.

2) Each CFV was installed between inlet and outlet pipes made of fiberglass filled PTFE with O-ring seals (see Figure 9). The PTFE material reduced conductive heat transfer between the heated CFV body and the approach pipe relative to the commonly used material, stainless steel. The thermal conductivity of PTFE is 1/60th that of stainless steel, but the cross-sectional area of the PTFE was 3.7 times that of a stainless steel approach pipe. This reduced heat flux due to the path labelled 2 in Figure 4 by a factor of 16.

3) Two thermistors with 3 mm diameter stainless steel sheaths were inserted through the wall of the approach pipe (T_1 and T_2 in Figure 9). Nylon compression fittings were used to reduce stem conduction errors (path 3 in Figure 4). The two thermistors were axially displaced from the CFV entrance plane by 40 mm (T_1) and 73 mm (T_2) to measure streamwise temperature changes as the gas approached the CFV entrance. We also used a 1.25 mm exposed bead thermister (T_z in Figure 9) that had a large immersion depth (> 300 mm) on the approach pipe centerline so that we could obtain gas temperature close to the CFV entrance plane with negligible error from stem conduction. We positioned the T_z sensor as close to the CFV entrance plane as practical: we made repeated $\dot{m}_{\mathrm{ref}}/\dot{m}_{\mathrm{CFV}}$ measurements at the same flow but with the sensor moved incrementally closer to the CFV entrance plane. Using the largest flow (3.2 mm CFV, at 700 kPa), we found that the T_z sensor did not alter $\dot{m}_{\mathrm{ref}}/\dot{m}_{\mathrm{CFV}}$ measurements by more than 0.02 % when located 10 mm from the entrance plane. The T_z measurements shown herein are all at that 10 mm position. The three gas temperature measurements, T_1, T_2, and T_z agreed with each other within 0.3 K for all of the experiments in this study and a temperature uncertainty of that magnitude introduces uncertainty in the $\dot{m}_{\mathrm{ref}}/\dot{m}_{\mathrm{CFV}}$ measurements of 0.05 %.

Two temperature sensors were inserted in oil-filled thermowells drilled into the CFV body (see Figure 8). One was a sheathed platinum resistance thermometer used as the input to a PID controlled heater to maintain the CFV at the desired T_{body} set point values. The other was an exposed bead thermistor. Both thermowells reached within 5.5 mm of the CFV centerline. A thin film 1.5 mm x 1.5 mm temperature sensor was taped to the exterior surface of the CFV body (T_{surf}), but the surface temperature measurements had large uncertainty.

Each of the 9 CFVs was calibrated with dry air (dew point temperature of 256 K) at 6 pressure setpoints (200 kPa to 700 kPa in 100 kPa increments). The discharge coefficient of the CFV was measured with uncertainty of 0.06 %, *k* = 2. A PID temperature controller and an electric heater wrapped around the CFV exterior were used to control T_{body} to nominal values of 298 K, 303 K, 308 K, and 313 K ± 0.9 K.

Three or more 34 L or 677 L *PVTt* collections were made at each pressure set point. Each *PVTt* flow collection (and averages of other sensor measurements) lasted between 0.3 min and 30 min. The data acquisition system also records log files of temperature and pressure measurements from numerous sensors with 10 s time resolution.

7. Data Processing

The calibration data consisted of the reference mass flow from the *PVTt* standard, the composition of the dried air, the static pressure (P_0) and temperature upstream (T_0 based on T_z) from the CFV, and the temperature of the CFV body. The corrections from static to stagnation pressure were all small (< 120 parts in 10^6) because the ratio of the approach pipe and throat diameters was > 6 for these experiments. We accounted for thermal expansion of the CFV throat using Equation 3.

The mass flow calculated via the CFV, accounting for thermal expansion of the CFV material is $\dot{m}_{\mathrm{R}*,\alpha} = C_{\alpha}\dot{m}_{\mathrm{R}*}$ and experimental values of this quantity for the Cu CFVs are plotted versus $Re^{-1/2}$ in Figure 10.

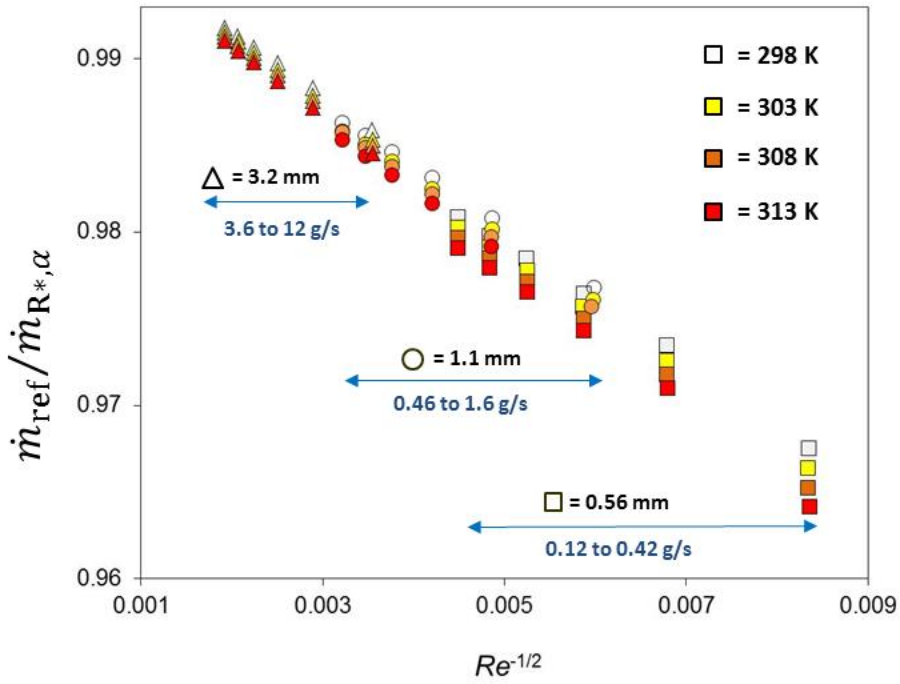

Figure 10. Discharge coefficient $\dot{m}_{\mathrm{ref}}/\dot{m}_{\mathrm{R}*,\alpha}$ for the Cu CFVs at body temperatures of 298 K, 303 K, 308 K, and 313 K.

The throat area at the reference temperature was calculated by fitting $\dot{m}_{\mathrm{ref}}/\dot{m}_{\mathrm{R}*}$ results for CFV body temperature of ≈298.15 K to analytical $C_{\mathrm{inv}}C_{\mathrm{vbl}}$ values based on Geropp [8] and Kleigel and Levine [6]. This fitting gave throat diameter and inlet curvature ratio Ω values that would be difficult to obtain by

dimensional metrology because the CFVs were all small (*d* = 3.2 mm or less). However, this fit to obtain *d* values was not critical: nominal values of *d* gives insignificantly different results for C_{T}.

For each CFV, the $\dot{m}_{\mathrm{ref}}/\dot{m}_{\mathrm{R}*,\alpha}$ values for the $T_{\mathrm{body}} = T_{\mathrm{ref}}$ = 298.15 K data set were fitted by a 3rd order polynomial of $Re^{-1/2}$. The residuals of the 3rd order fit were always less than 65 parts in 10^6 while the residuals for a 2nd order fit were as large as 130 ppm. We conclude that there are significant 2nd ***and*** 3rd order dependencies of $\dot{m}_{\mathrm{ref}}/\dot{m}_{\mathrm{R}*,\alpha}$ on $Re^{-1/2}$ for CFVs of the size in this study.

The fits to $\dot{m}_{\mathrm{ref}}/\dot{m}_{\mathrm{R}*,\alpha}$ values at $T_{\mathrm{body}} = T_{\mathrm{ref}}$ were used to calculate $\Delta\,\dot{m}_{\mathrm{ref}}/\dot{m}_{\mathrm{R}*,\alpha} = \dot{m}_{\mathrm{ref}}/\dot{m}_{\mathrm{R}*,\alpha}\left(T_{\mathrm{body}}\right) - \dot{m}_{\mathrm{ref}}/\dot{m}_{\mathrm{R}*,\alpha}\left(T_{\mathrm{ref}}\right)$ for calibration data collected at T_{body} = 298 K, 303 K, 308 K, and 313 K. We assumed that thermal boundary layer effects are sufficiently small and could be combined linearly with other CFV corrections and calculated a thermal boundary layer correction:

$$C_{\mathrm{T}} \cong 1 + \left[\frac{\dot{m}_{\mathrm{ref}}}{\dot{m}_{\mathrm{R}*,\alpha}(T_{\mathrm{body}})} - \frac{\dot{m}_{\mathrm{ref}}}{\dot{m}_{\mathrm{R}*,\alpha}(T_{\mathrm{ref}})}\right] \tag{4}$$

Note that $\dot{m}_{\mathrm{ref}}/\dot{m}_{\mathrm{R}*,\alpha}$ is equivalent to an experimental measurement of $C_{\mathrm{inv}}C_{\mathrm{vbl}}$ (often called C_{d}) and Equation 4 corrects for changes in this quantity for various values of T_{body} (or T_{wall}).

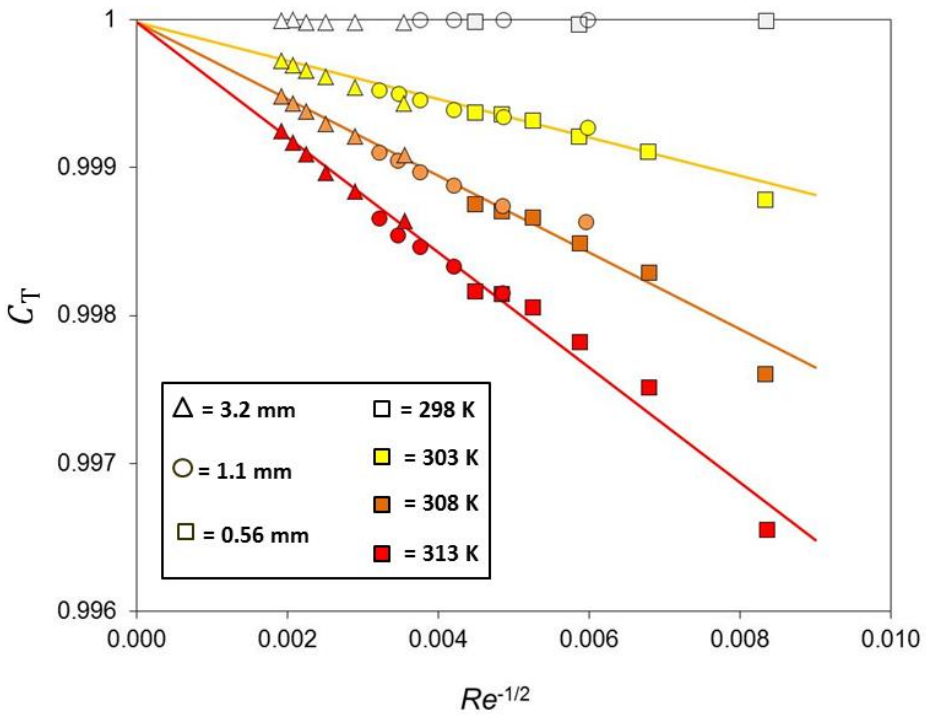

Figure 11. C_{T} for various throat diameters and body temperatures plotted versus $Re^{-1/2}$ using the same data as in Figure 10.

8. Experimental Results

Figure 10 plots the discharge coefficient with thermal expansion corrections ($\dot{m}_{\mathrm{ref}}/\dot{m}_{\mathrm{R*,inv,vbl},\alpha}$) for the three copper CFVs at four CFV body temperatures. The discharge coefficient $\dot{m}_{\mathrm{ref}}/\dot{m}_{\mathrm{R*,inv,vbl},\alpha}$ decreases with increasing body temperature and the effect is more pronounced for smaller Reynolds number. Figure 11 plots values of C_{T} calculated from Equation 4 and the data of Figure 10. For each nominal T_{body} set point, a linear function of $Re^{-1/2}$ fits the results for three different throat diameter CFVs within ± 0.0002.

It is worth noting that the $C_{\mathrm{R}}^{*}C_{\mathrm{inv}}C_{\mathrm{vbl}}$ model (and the adiabatic wall assumption) does not ignore the thermal boundary layer: instead the boundary layer is heated only by viscosity and not by heat transfer from the wall. The adiabatic assumption is only an approximation. In most applications, the wall of a thermally conductive CFV is warmer than the adiabatic wall temperature and for Re < 10^6, there is a significant heat flux from the CFV body into a thermal boundary layer. The thermal boundary layer is warmer than the free stream (or core flow) and its lower density leads to less mass flux through the CFV and hence lower $\dot{m}_{\mathrm{ref}}/\dot{m}_{\mathrm{R*,inv,vbl},\alpha}$ values. We also know from theory that the laminar thermal boundary layer scales with $Re^{-1/2}$ [25] and so does C_{T} (theoretically and experimentally).

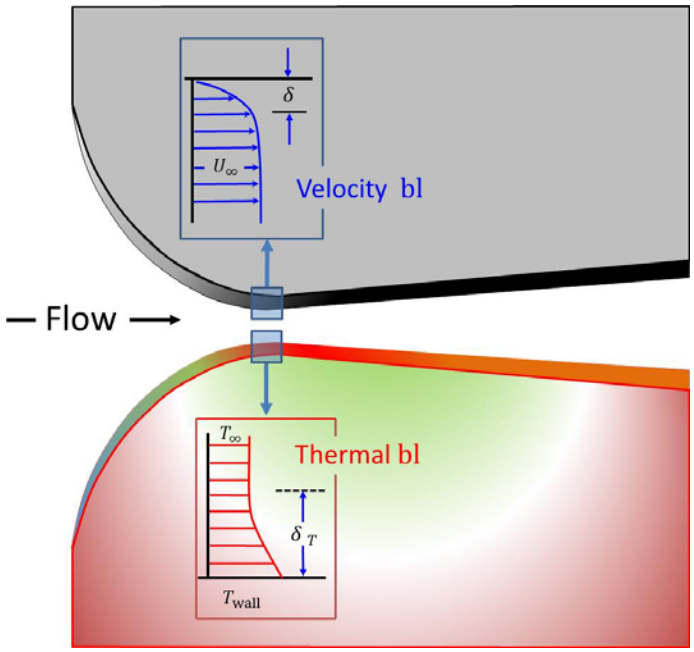

Figure 12. Schematic representation of the velocity and thermal boundary layers in a critical flow venturi.

Because the thermal boundary layer thickness scales with $Re^{-1/2}$ and the density change of the gas in the thermal boundary layer scales with $\Delta T/T_0$, we propose an expression for C_{T}:

$$C_{\mathrm{T}} = 1 + KRe^{-1/2}\left[\frac{\Delta T}{T_0}\right]. \quad (5)$$

where K is a dimensionless proportionality constant and $\Delta T = T_{\mathrm{wall}} - T_0$. For the experiments in this study conducted with metal CFVs, $T_{\mathrm{body}} \approx T_{\mathrm{wall}}$ and we have used $T_{\mathrm{body}} - T_0$ to approximate ΔT. A plot of C_{T} calculated from experimental data via Equation 4 versus $Re^{-1/2}\,(\Delta T)/T_0$ for the Cu CFVs is shown in Figure 13.

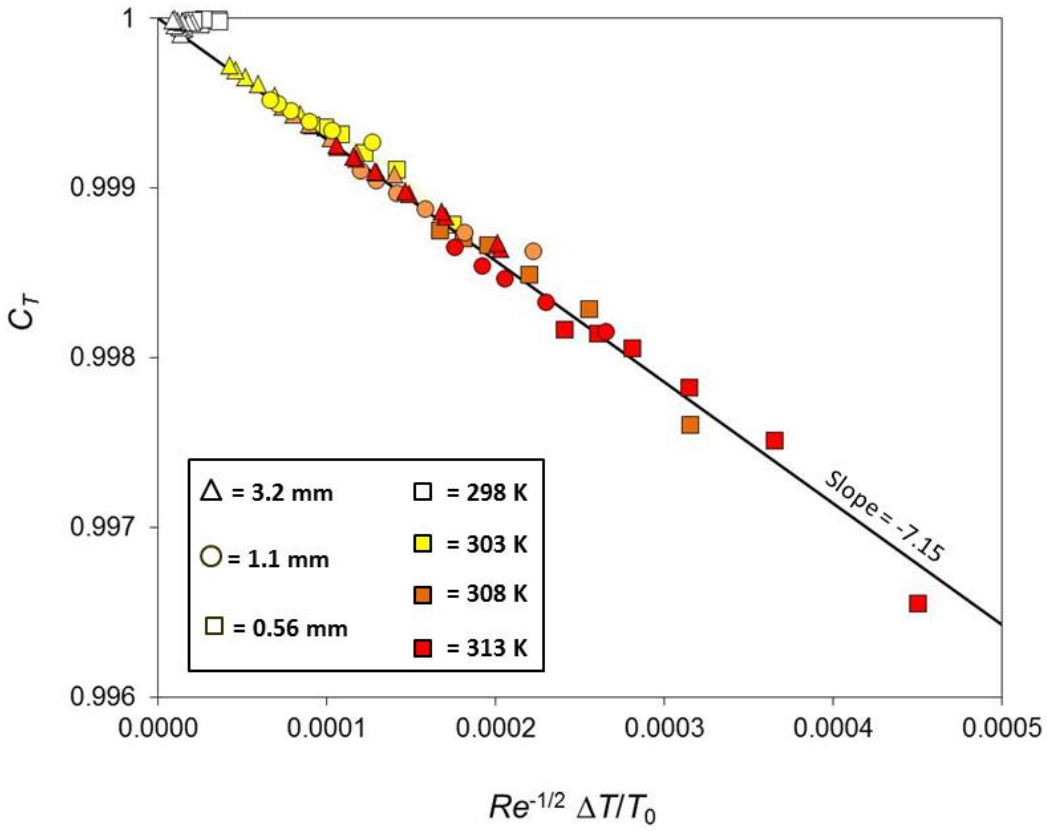

Figure 13. C_{T} versus $Re^{-1/2}\,(\Delta T)/T_0$ for the Cu CFVs using the same data in Figures 10 and 11.

Results for the three stainless steel CFVs are shown in Figure 14. The offset in the 3.2 mm data relative to the other two CFVs is likely due to increasing differences between T_{body} and T_{w} for this particular CFV because 1) it produces the largest flows and hence the greatest heat flux from the CFV body into the flowing gas and 2) SS is less thermally conductive than Cu. The Biot number is large: for the largest SS CFV, the convective heat transfer from the CFV to the gas is large and the thermal conductivity of SS is lower than that of copper. Although T_{body} is controlled, it is displaced from the wall and the temperature gradient is significant. This leads to T_{wall} being several degrees cooler than T_{body} and a measured value of C_{T} that is closer to unity. Ignoring the 3.2 mm data, the slope (K) of the SS data in Figure 14 and the Cu data in Figure 13 is -7.15. The slope for the 3.2 mm SS CFV data is -5.05.

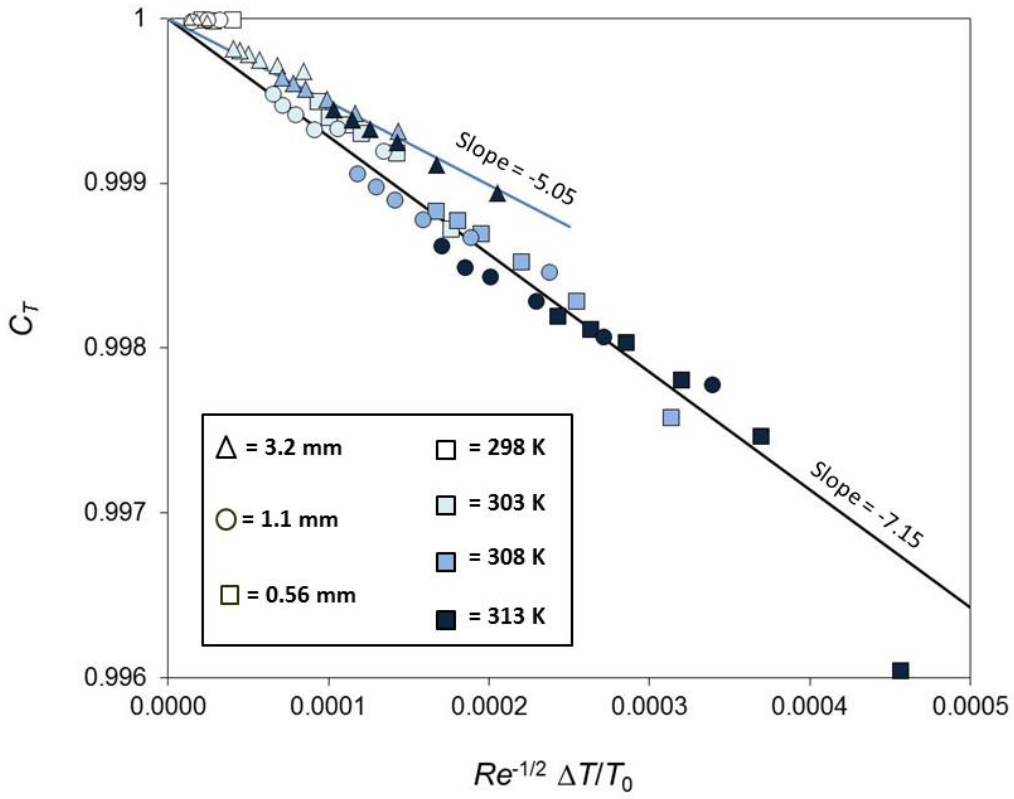

Figure 14. C_{T} versus $Re^{-1/2}\ (\Delta T)/T_0$ for the SS CFVs.

9. Discussion and Conclusions

Temperature sampling errors are the largest concern when trying to achieve CFV flow measurements that are reproducible under variable room temperature or gas temperature conditions. The gas expanding through the CFV cools the CFV body and connecting piping which causes temperature gradients in the gas and can lead to stem conduction errors in the gas temperature sensor. In these experiments, to minimize temperature sampling errors, we used a heat exchanger for the incoming gas (297 K ± 0.7 K), controlled the room temperature (297 K ± 0.3 K), used insulating pipe materials to reduce heat conduction, and placed a long stemmed temperature sensor only 10 mm from the CFV entrance. These design efforts improved the measurement of T_0: the temperature differences between T_1 and T_Z were < 0.25 K, smaller than for the normal installation configurations we use. A 0.25 K temperature uncertainty affects CFV mass flow result by 0.04 %. The temperature sampling errors were generally larger for the smaller CFVs and at lower mass flows. We suspect that even with the T_Z sensor placed as close as 10 mm from the CFV entrance plane, there are significant temperature changes in the gas before it enters the CFV.

Mass flow through a CFV is predictably sensitive to the temperature of the CFV body and **thermal effects can be accounted for** using the equation:

$$\dot{m}_{\mathrm{CFV}} = \frac{C_{\mathrm{inv}} C_{\mathrm{vbl}} C_{\alpha} C_{\mathrm{T}} P_0 A C_{\mathrm{R}}^{*} \sqrt{M}}{\sqrt{R T_0}}, \tag{6}$$

where C_{T}, the correction to the CFV model accounting for the thermal boundary layer can be calculated by $C_T = 1 + KRe^{-1/2}[\Delta T/T_0]$ where ΔT is $T_{\mathrm{wall}} - T_0$. For metal CFVs, T_{body} is a good approximation for T_{wall}. Figure 3 illustrates that for a *d* = 0.58 mm CFV subjected to a 5 K room temperature change, a 5-fold improvement in flow measurements is possible when corrections for thermal effects are applied. Note that the value of K used in Figure 3 was -11.5, rather than the -7.07 value measured during the controlled CFV body temperature experiments. While K = -7.07 is the best fit value for the entire data set in Figure 13, the K value for $Re^{-1/2}\,(\Delta T)/T_0$ = 0.0004 (the value for the data in Figure 3) is also approximately -11.5 due to local curvature of the data.

Obtaining a **good estimate of T_{wall} is necessary** for calculating C_{T}. In our case a thermowell in the CFV body and a bead thermistor were used to measure T_{body} and we assumed that $T_{\mathrm{body}} \approx T_{\mathrm{wall}}$. For a reasonably conductive CFV material (Cu or SS), this works well. But our models and experimental evidence indicate that we know T_{wall} only within 3 K for a stainless steel CFV. Based on Figure 11, a 3 K error in T_{wall} leads to 0.06 % error in C_{T}. We know that the difference between the measured T_{body} and T_{wall} grows with decreasing thermal conductivity of the CFV material and is a function of the Reynolds number (or flow). Better estimates of T_{wall} can be made by using a conductive material, like Cu, or by making two temperature measurements at precisely known depths in the CFV body and using the expected logarithmic relationship between radial depth versus temperature to calculate extrapolated values of T_{wall}.

Another idea is to **construct the CFV from a material with low thermal conductivity** (i.e. ceramic). This leads to a large Biot number and more closely approximates the adiabatic wall used in analytical C_{vbl} calculations. We constructed CFVs from a machinable ceramic material that has thermal conductivity of 1.46 W/m-K. Unlike the Cu or SS CFVs, the low thermal conductivity of ceramic means that the CFV body temperature measured in the thermowell is not a good approximation of the wall temperature (15 K for our design). To make the materials comparison more consistent, the CFVs made of Cu, SS, and ceramic were tested with controlled external surface temperatures using an electric heater and a 1.5 mm x 1.5 mm thin film temperature sensor placed between the CFV surface and the electric heater. Even with thermally conductive grease between the CFV and the heater, it is difficult to acquire low uncertainty surface temperature measurements and the results of these tests are not as clear as when the CFV body temperature was controlled. But the sensitivity of the CFV mass flow to the surface temperature changes (K) was approximately 30 % smaller for the ceramic CFVs than for the metal CFVs.

In another test, we placed the CFV in a temperature controlled box and changed the temperature from 296 K to approximately 303 K. The results for Cu and ceramic CFVs with *d* = 0.56 mm and *Re* = 2.3 x 10^4 are shown in Figure 15. The box did not cover the approach pipe. T_Z was higher and took longer to reach steady state for the Cu CFV, probably because the lower thermal conductivity of the ceramic

reduced the heat transfer via path 2 in Figure 4. The changes in mass flow for the commonly used $C_{\mathrm{inv}}C_{\mathrm{vbl}}$ correction are smaller despite the 1 K higher box and CFV body temperatures (as one would expect based on the smaller K values for ceramic). Therefore, the ceramic material is less sensitive to environmental temperature changes, but not markedly so. This can be understood by noting that the wall temperatures for ceramic CFVs shown in Figure 7 are cooler than for the metal CFVs, but still considerably warmer than the adiabatic wall temperature. Therefore there is little to be gained by replacing metal CFVs with ceramic ones. Instead we must correct for or control the environment.

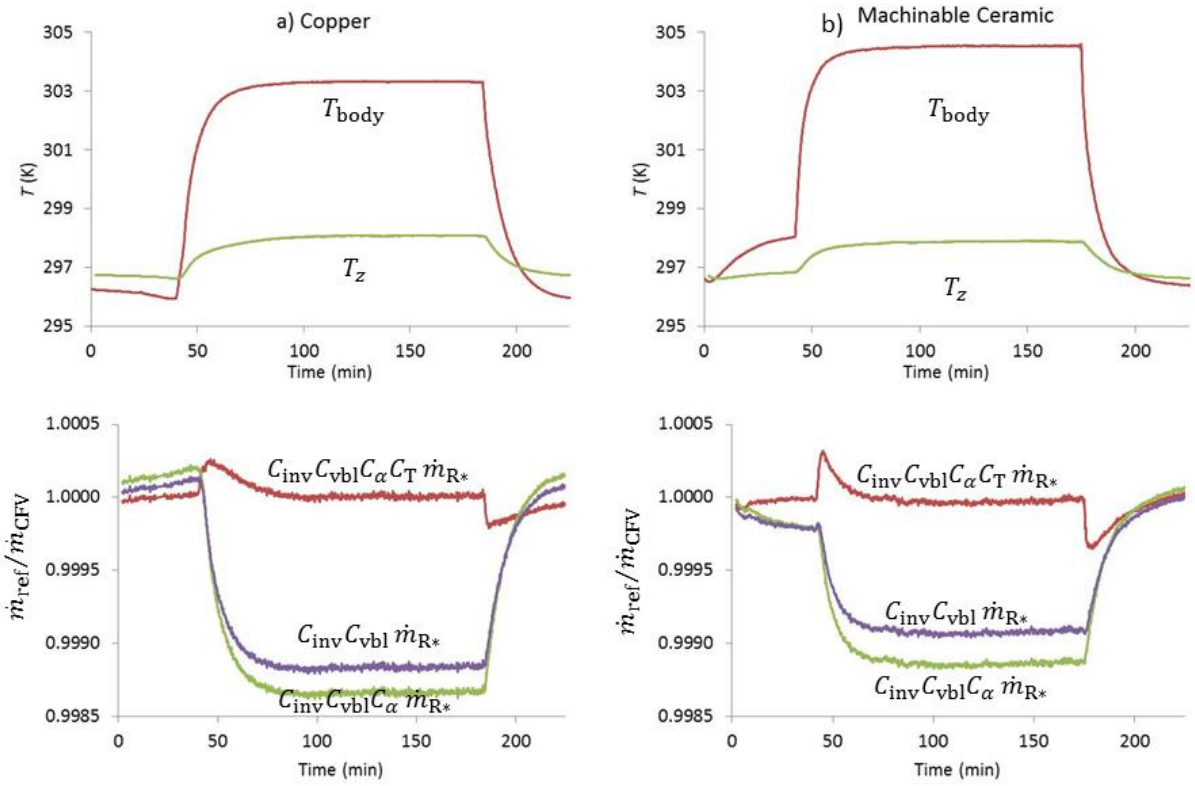

Figure 15. Comparison of the effects of heating the environment surrounding a *d* = 0.56 mm at CFV *Re* = 2.3 x 10^4 and the various flow calculation approaches for a) a copper CFV and b) a machinable ceramic CFV.

Figure 16 is a time trace of temperatures with 10 s resolution showing 17 *PVTt* collection cycles at 6 increasing pressure set points. As expected, the Cu CFV body temperature decreases as the upstream pressure set point is raised and the cooling due to gas expansion increases. It is normally assumed that CFVs used in the critical flow condition are unperturbed by the change in downstream pressure that occurs as a *PVTt* collection tank fills from near vacuum to its full pressure, in this case 100 kPa. Figure 16 shows that the **CFV body temperature changes during a *PVTt* flow measurement.** The CFV body temperature transients are caused by the changing pressure drop across the CFV: there is greater cooling due to expansion at the beginning of a collection when the CFV downstream pressure is near vacuum than when the tank is full or the flow is bypassed to the room (100 kPa). Also, the effect is more pronounced at lower values of P_0 because the relative pressure change caused by the filling tank is

greater. The change in magnitude of the cooling with P_0 may also be related to shocks changing position in the diverging section of the CFV.

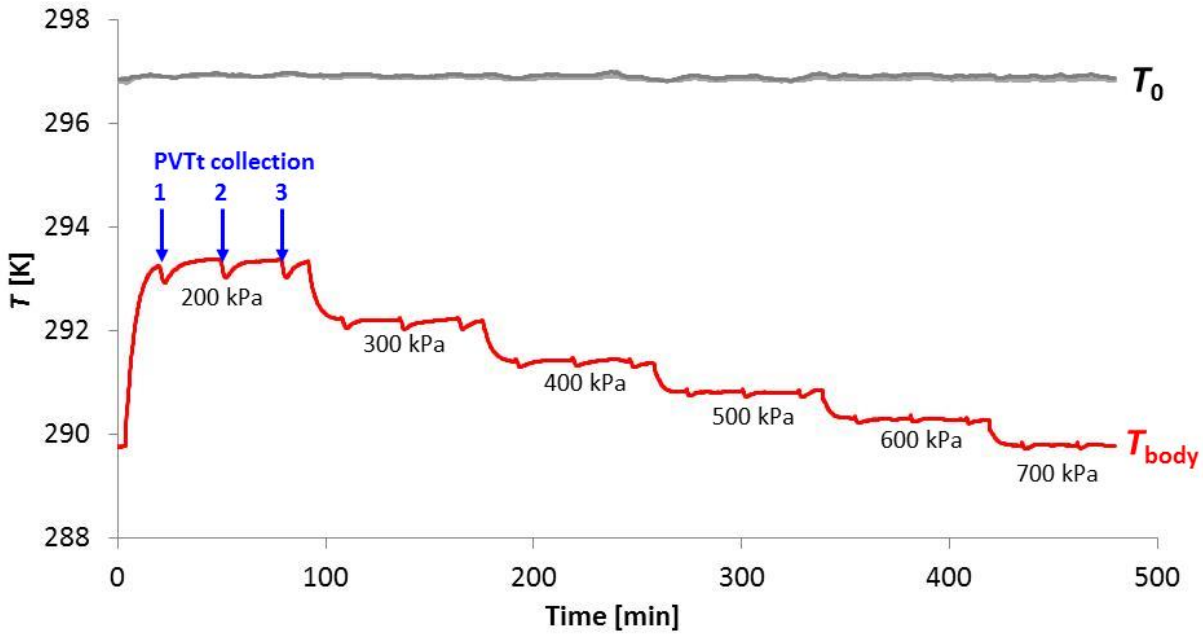

Figure 16. Time traces of CFV temperatures during sequential *PVTt* collections at pressure setpoints of 200 kPa to 700 kPa in 100 kPa increments. The T_{body} dips are due to changes in the cooling due to gas expansion when the collection tank is filled.

Bignell and Choi [21] calibrated four heated CFVs and we have used Figure 6 in their publication to calculate C_{T} values. Their results are plotted in Figure 17a along with the Cu CFV data in the same format as Figure 11. The decrease in flow as the CFV body temperature is raised is similar to our results for their largest (d = 2mm) CFV, but the effects are larger for the smaller CFVs and are not linear with $Re^{-1/2}$. We also observed similar (but less pronounced) nonlinear effects in our data at large $Re^{-1/2}$values.

Figure 17b presents Bignell and Choi's C_{T} values versus $Re^{-1/2}$ $(\Delta T)/T_0$ along with data produced in our lab for a prior iteration of the experiments described in this publication (NIST 2013 data). In these experiments, the CFVs were made of Cu, but the approach pipe was not as well thermally isolated from the heated CFV. The solid line in Figure 17b with slope = -7.07 represents the Cu CFV results from Figure 13. Both Bignell and Choi's and the NIST 2013 data do not agree with the results of this study, but do show similar trends. The source of this disagreement and the non-linearity in Figure 17a is unclear, but one possibility is temperature sampling errors are a more significant problem for the smaller CFVs. Perhaps at these low Re values, the residence time of the gas near the CFV entrance plane is long enough that heat conduction from the hot CFV body through the gas is causing errors in the

measurement of T_0. Note that if the actual T_0 is higher than the measured value, smaller experimental values of C_T will be observed.

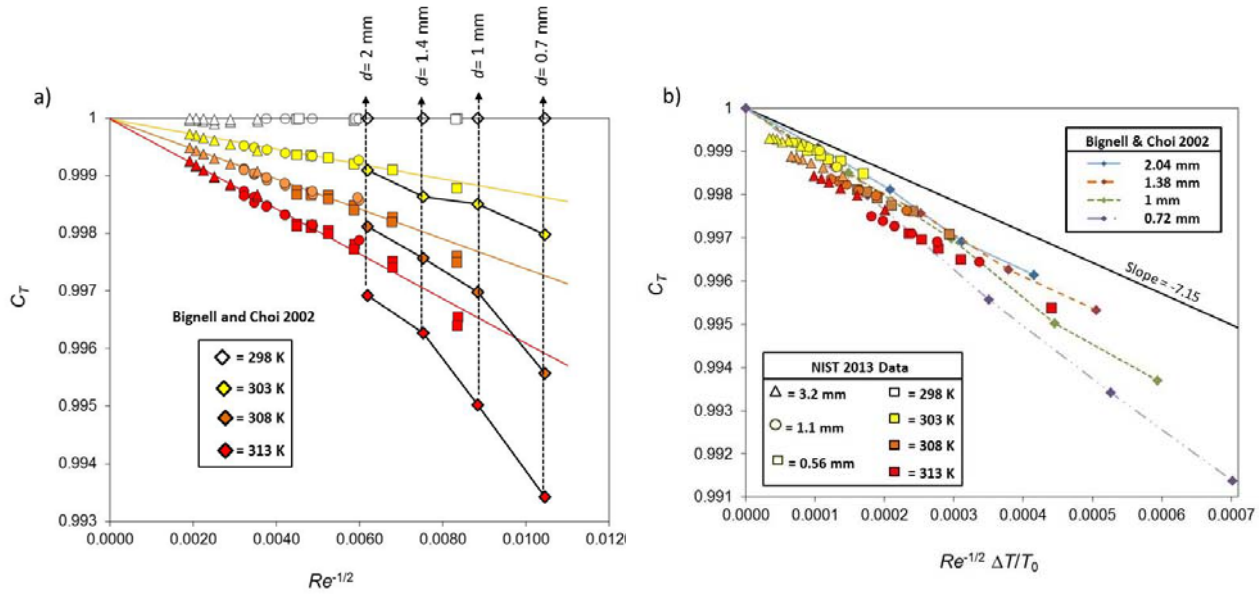

Figure 17. Prior experimental results for C_T. a) Bignell and Choi's results versus $Re^{-1/2}$ along with Cu CFV results from this work. b) Bignell and Choi's results and NIST data for a different experimental design conducted in 2013.

We have arrived at Equation 5 heuristically, but similarity transformations and integral methods have been successfully applied to thermal boundary layer problems [26, 27] and we expect **fluid dynamicists can improve our model for C_T**. Johnson [28] used CFD to calculate the change in CFV flow between a "hot wall" and adiabatic wall (see his Figure 3.11). In that work, Johnson notes that thermal boundary layer effects are larger for gases with large specific heat ratios: large γ causes lower free stream temperature T_{core} and therefore increased heat transfer from the CFV wall. We also speculate that C_T may have some dependence on the CFV inlet curvature ratio Ω: larger inlet curvature will lead to a thicker thermal boundary layer at the throat and smaller C_T values. While we have utilized $(T_{body} - T_0)/T_0$ in this work as a practical ratio to account for gas density changes in the boundary layer, the expression $(T_{wall} - T_{aw})/T_{aw}$ is more appropriate for theoretical analysis of the thermal boundary layer correction.

As a researcher, it is frustratingly difficult to separate and measure C_T and temperature sampling effects, but as an engineer, perhaps that is not so important. We conclude that values of K (and for the y-axis intercept) for various installation configurations (i.e. materials, insulation, external T conditions, boundary conditions) are likely to differ, but note that **Equations 5 and 6 fit well for various CFV installation configurations**. A practical approach to applying the results of this paper is to use a thermally conductive CFV material, measure T_{body} in the configuration that is to be used later, control the heat transfer paths shown in Figure 4, and apply Equations 5 and 6. When this approach is applied to the NIST 2013 data in Figure 17b), the C_T residuals are < 0.05 % and have standard deviation of 0.025 %.

It is worth noting that if one controls T_{body} and T_0 during calibration and usage, effects due to C_α and C_T are constant. Hence a practical approach to highly improved gas flow reproducibility is to control the CFV body, approach pipe, and gas temperatures with PID controlled Peltier effect heaters/coolers and use the same temperature set point during calibration and usage.

Fits to CFV calibration data show smaller residuals when they include both a $Re^{-1/2}$ and Re^{-1} term (i.e., when a 2nd order polynomial in $Re^{-1/2}$ is applied) and the Re^{-1} term is more important for smaller *Re* number. This can be explained by considering the velocity boundary layer displacement thickness δ^*: the fractional reduction in the cross sectional area of flow at the throat is:

$$C_{\mathrm{vbl}} = \frac{[\pi(d-2\delta^*)^2/4]}{[\pi d^2/4]} = 1 - 4\frac{\delta^*}{d} + 4\left(\frac{\delta^*}{d}\right)^2. \quad (7)$$

Because δ^* is a function of $Re^{-1/2}$, the last term in Equation 7 leads to a Re^{-1} functionality [28, 29].

A close examination of the data in Figures 13 and 14 gives the impression that there is a **3rd order behavior of C_T**. Fits to C_T show increasing absolute values for the 3rd order coefficient as T_{body} increases. One approach to understanding changes in $C_{\mathrm{inv}}C_{\mathrm{vbl}}$ and C_T is to consider $C_{\mathrm{inv}}C_{\mathrm{vbl}}$ as Geropp, Tang, and Kleigal and Levine have expressed for a laminar boundary layer:

$$[C_{\mathrm{inv}}C_{\mathrm{vbl}}]_{\mathrm{aw}} = 1 + a_1\Omega^{-1/4}Re^{-1/2} + a_2\Omega^{-1/2}Re^{-1}, \quad (8)$$

where Ω is the CFV inlet curvature ratio, and then postulate the discharge coefficient for a boundary layer with heat transfer as:

$$[C_{\mathrm{inv}}C_{\mathrm{vbl}}]_{\mathrm{hot}} = 1 + b_1\Omega^{-1/4}Re^{-1/2} + b_2\Omega^{-1/2}Re^{-1}, \quad (9)$$

Which leads to:

$$C_\mathrm{T} = \frac{[C_{\mathrm{inv}}C_{\mathrm{vbl}}]_{\mathrm{hot}}}{[C_{\mathrm{inv}}C_{\mathrm{vbl}}]_{\mathrm{aw}}} = 1 + (b_1 - a_1)Re^{-1/2} + (b_2 - a_2 - a_1b_1)Re^{-1} - (a_2b_1 + a_1b_2)Re^{-3/2} - a_2b_2Re^{-2}, \quad (10)$$

Indicating that 3rd and even 4th order $Re^{-1/2}$ dependence can be expected in C_T .

Acknowledgements: This work was partially supported by a Cooperative Research and Development Agreement with Colorado Engineering Experiment Station, Inc. and their subsidiary Flow Systems, Inc. We also wish to acknowledge Gina Kline of the NIST Fluid Metrology Group for her assistance in the laboratory.

[1] Lemmon E. W., Huber M. L., and McLinden M. O., *NIST Standard Reference Database 23: Reference Fluid Thermodynamic and Transport Properties-REFPROP*, Version 9.0 National Institute of Standards and Technology, Standard Reference Data Program, Gaithersburg, 2007.

[2] Wright, J., Mickan, B., Paton, R., Park, K.-A., Nakao, S.-I., Chahine, K., Arias, R., *CIPM Key Comparison for Low Pressure Gas Flow: CCM.FF-K6 Final Report*, Metrologia, 44, 07007, 2007.

[3] International Standards Organization, *Measurement of Gas Flow by Means of Critical Flow Venturi Nozzles*, ISO 9300, 2nd edition, 2005.

[4] Anderson, J. D., *Modern Compressible Flow*, 3rd ed., McGraw Hill, 2004.

[5] Hall, G. W., *Transonic Flow in Two-Dimensional and Axially-Symmetric Nozzles*, Quart. Journal Mech. and Applied Math., 15, pp. 487 – 508, 1962.

[6] Kliegel, J. R. and Levine, J. N., *Transonic Flow in Small Throat Radius of Curvature Nozzles*, AIAA Journal, 7, pp. 1375-1378, 1969.

[7] Tang, S. P., *Discharge Coefficients for Critical Flow Nozzles and Their Dependence on Reynolds Number*, Ph. D. Thesis Princeton University, Princeton, New Jersey, USA, 1969.

[8] Geropp, D., *Laminare Grenzschichten in Ebenen und Rotationssymmetrischen Lavaldusen*, Deutsche Luft- und Raumfahrt Forschungsbericht, pp. 71 – 90, 1971.

[9] Stratford, B. S., *The Calculation of the Discharge Coefficient of Profiled Choked Nozzles and the Optimum Profile for Absolute Air Flow Measurement*, Journal of the Royal Aeronautical Society, 68, pp.237 – 245, 1964.

[10] Mickan, B., *Determination of Discharge Coefficient of Critical Nozzles Based on Their Geometry and the Theory of Laminar and Turbulent Boundary layers*, 6th International Symposium for Fluid Flow Measurement, Queretaro, Mexico, B.2.1, 2006.

[11] Johnson, A. N. and Wright, J. D., *Comparison between Theoretical CFV Models and NIST's Primary Flow Data in the Laminar, Turbulent, and Transition Flow Regimes*, ASME Journal of Fluids Engineering, vol. 130, July, 2008.

[12] Wright, J. D., *The Long Term Calibration Stability of Critical Flow Nozzles and Laminar Flowmeters*, Proceedings of the NCSL Workshop and Symposium, Albuquerque, New Mexico, USA, pp. 443 – 462, 1998.

[13] Wright, J. D., Johnson, A. N., Moldover, M. R., and Kline, G. M*., Gas Flowmeter Calibrations with the 34 L and 677 L PVTt Standards*, NIST Special Publication 250-63, National Institute of Standards and Technology, Gaithersburg, Maryland, November 18, 2010.

[14] Wright, J. D., Kayl, J.-P., Johnson, A. N., and Kline, G. M., *Gas Flowmeter Calibrations with the Working Gas Flow Standard*, NIST Special Publication 250-80, National Institute of Standards and Technology, Gaithersburg, MD, November 23, 2009.

[15] Carter, M., Johansen, W., Britton, C., *Performance of a Gas Flow Meter Calibration System Utilizing Critical Flow Venturi Standards*, Proceedings of FLOMEKO, Taipei, Taiwan, 2010.

[16] Ishibashi, M., Morioka, T., and Arnberg, B. T., *Effect of Inlet Curvature on the Discharge Coefficients of Toroidal-Throat Critical-Flow Venturi Nozzles*, FEDSM2005-77470, Proceedings of the ASME Fluids Engineering Summer Meeting, Houston, Texas, USA, 2005.

[17] Wright, J. D., *Uncertainty of the Critical Venturi Transfer Standard Used in the K6 Gas Flow Key Comparison*, Proceedings of FLOMEKO, Johannesburg, South Africa, 2007.

[18] Jones E. H., *Material Temperature Profiles in a Critical Flow Nozzle*, ASME Winter Annual Meeting, Chicago, Illinois, USA, Nov. 27 to Dec. 2, 1988.

[19] Caron, R. W. and Carter, M. S., *Temperature Profile within Sonic Nozzles*, 3rd International Symposium on Fluid Flow Measurement, San Antonio, Texas, USA, 1995.

[20] Kegel, T. M. and Caron, R. W., *Some Effects of Thermal Phenomena on the Accuracy of CFV Based Flowrate Measurements*, Proceedings of the ASME Fluids Engineering Summer Meeting, San Diego, California, USA, 1996.

[21] Bignell, N. and Choi, Y. M., *Thermal Effects in Small Sonic Nozzles*, Flow Meas. Instrum., 13, pp. 17 – 22, 2002.

[22] Johnson, A. N., Merkle, C. L., Espina, P. I., Mattingly, G. E., and Wright, J. D., *Numerical Characterization of the Discharge Coefficient in Critical Nozzles*, Proceedings of the NCSL Workshop and Symposium, Albuquerque, New Mexico, USA, pp. 407 – 422, 1998.

[23] Pope, J. G. and Wright, J. D., *Performance of Coriolis Meters in Transient Gas Flows*, Flow Measurement and instrumentation, Volume 37, pp. 42 – 53, 2014.

[24] Smith, A. G. and Spalding, D. B., *Heat Transfer in a Laminar Boundary Layer with Constant Fluid Properties and Constant Wall Temperature*, J. Royal Aeronautical Soc., 62, pp. 60 - 64, 1958.

[25] Bejan, A., *Heat Transfer*, Section 2.2, John Wiley and Sons, 1993.

[26] White, F. M, *Viscous Fluid Flow*, Chapter 7, McGraw Hill, 1974.

[27] Cohen, C. B. and Reshotko, E., *The Compressible Laminar Boundary Layer with Heat Transfer and Arbitrary Pressure Gradient*, NACA Report 1294, 1956.

[28] Johnson, A. N., *Numerical Characterization of the Discharge Coefficient in Critical Nozzles*, Ph.D. Thesis, Pennsylvania State Univ., University Park, Pennsylvania, USA, 2000.

[29] Mickan, B., *The Use of Micro-Nozzles under Sonic and Subsonic Conditions with Various Gases*, 6th International Symposium for Fluid Flow Measurement, Queretaro, Mexico, B.2.3, 2006.